Digital Twin of a High-Speed Billet Caster



Digital technologies are transforming industry at all levels. Steel has the opportunity to lead all heavy industries as an early adopter of specific digital technologies to improve our sustainability and competitiveness. This column is part of AIST's strategy to become the epicenter for steel's digital transformation, by providing a variety of platforms to showcase and disseminate Industry 4.0 knowledge specific for steel manufacturing, from big-picture concepts to specific processes.

Authors

Zhikai Liu (top left), Ph.D. Candidate, Department of Materials Science and Engineering Center for Iron and Steelmaking Research, Carnegie Mellon University, Pittsburgh, Pa., USA
zhikaili@andrew.cmu.edu

Bryan Webler (top right), Professor, Department of Materials Science and Engineering Center for Iron and Steelmaking Research, Carnegie Mellon University, Pittsburgh, Pa., USA
bwebler@andrew.cmu.edu

P. Chris Pistorius (bottom), POSCO Professor of Materials Science and Engineering and Co-Director, Center for Iron and Steelmaking Research Carnegie Mellon University, Pittsburgh, Pa., USA
pcp@andrew.cmu.edu

Introduction

Continuous casting is a vital steel manufacturing process in which molten steel is continuously poured into a water-cooled mold at the top of a caster. As it descends, solidification begins at the outer shell and progresses inward until the entire section solidifies. This method enhances efficiency and ensures uniform solidification, making it a superior alternative to traditional ingot casting. The origins of continuous casting date back to the 1930s when Junghans demonstrated its potential to reduce steel losses by 10–20% compared to ingot mold casting.[1] Over time, technological advancements have refined the process, making it the dominant method in modern steel production, now accounting for approximately 96% of global steel output.[2] Among various casting techniques, micro-mills have emerged as a cost-effective option, particularly when customers and scrap suppliers are close.[3]

A micro-mill is a type of steel mill with compact casters that demands high production reliability.[2,4] During typical operations, the cast strand feeds directly into the hot rolling mills; however, billets can be sheared prior to the hot mill if necessary. It is critical that solidification is complete by the shear position, otherwise a breakout could occur on shearing.

Preventing shear-related breakouts depends on accurately predicting the metallurgical length during production. However, the solidification endpoint, which defines the metallurgical length, is difficult to measure directly. The current approach to avoiding breakouts is reducing casting speed, but this strategy also lowers yield. To overcome these challenges and improve casting efficiency, digital twin technology offers a promising solution by enhancing metallurgical length prediction.

A digital twin is a concept that links a cyber model to the physical world, enabling real-time interactions between them. By 2016, advancements in cloud computing, the Internet of Things (IoT) and big data revitalized digital twin technology, sparking a surge in research publications and growing interest from both industry and academia.[5]

Digital twins can be classified into two main types based on scale and function: local and global. Local digital twins focus on simulating specific assets and their immediate environment, while global digital twins combine multiple local twins to provide a comprehensive, system-wide simulation.[6] A typical digital twin framework is shown in Fig. 1.[6]

As shown in Fig. 1, a five-layer digital twin framework includes the following layers: a cyberphysical data storage layer, a primary processing layer, a models and algorithms layer, an analysis layer, and a user interface layer.[7] Each layer represents a step in processing data from the layer above and delivers the result to the layer below. Real-time data from detectors in the physical system is stored in the cyberphysical data storage layer and processed through the digital twin to provide real-time feedback. Meanwhile, historical data is used to refine the model in the digital twin models and algorithms layer.

Integrating digital twins into micro-mill casters can enhance production quality and minimize risks by providing precise simulations that support the continuous casting process. It also improves safety by reducing the likelihood of steel breakouts at shear. In this work, a digital twin was developed that combines a physical model with a data-driven digital model. This system can accurately predict the steady-state metallurgical length of the caster in real time.

Methods

This section details the structure of the digital twin model. In the approach, caster and operation parameters are first fed into a cyberphysical data storage layer. The model then uses caster and operation parameters to initialize the simulation. Once it is initialized, the model calculates the metallurgical length at different superheats and mold water cooling temperatures. Then superheat, mold water cooling temperatures and casting speeds will be fed into a surrogate model to calculate metallurgical lengths. The overall structure of the digital twin model is shown in Fig. 2.

Caster Information

The micro-mill caster includes a mold cooling zone and seven spray cages that apply water to the steel surface, helping maintain a near-constant surface temperature during billet solidification. The caster schematic is shown in Fig. 3.

Information on the steel and caster specifications was obtained from an industry partner. The steel composition

Figure 1

Architecture of a five-layer digital twin. Solid lines indicate the direction of execution, while dashed lines represent the direction of data extraction.

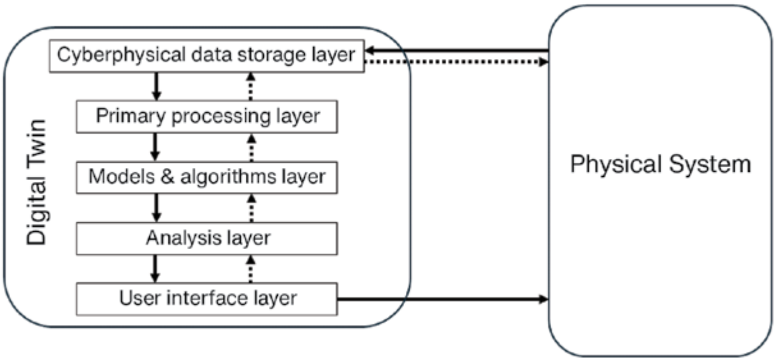

Figure 2

Components and high-level processes of digital twin.

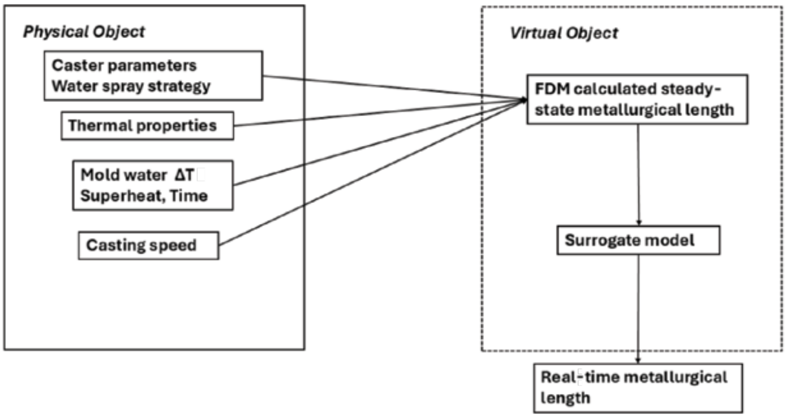

Figure 3

The scheme of a micro-mill caster. Region labels represent billet travel distance given by supplier. Mold working length is 0.87 m.

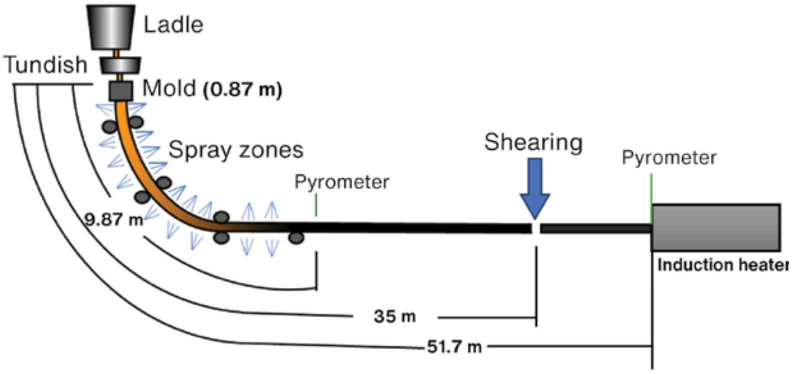

Table 1

Spray Cage Lengths

Cage number	1	2	3	4	5	6	7
Length (m)	0.3	0.5	1.0	2.0	2.0	2.0	1.2

is Grade 60 steel with 0.25% carbon. Other grades are possible; however, this work focuses only on Grade 60. In the spray cooling zone, there are seven different spray cages with different spray nozzle configurations; the lengths for each spray cage are shown in Table 1.

Heat transfer occurs through convection-radiation and conductive cooling in the mold and spray cooling zones; after the billets exit the water spray cooling area, the convection-radiation makes a major contribution. The boundary conditions for these zones are determined by analyzing heat transfer on the hot metal surface.[12] In the mold cooling zone, heat transfer from the billet is driven by water flow through the mold which has 870 mm working length, while in the spray cooling zone, it depends on water flux from the spray nozzles.

Heat extraction in both the mold and spray cooling zones is tied to the casting speed. The heat flux from water spray cooling is calculated based on the water flux area, which is the billet surface covered by spray nozzle. Calculated heat flux in primary and secondary cooling zones is shown in Fig. 4.

Table 2 summarizes the boundary conditions used in each zone.

Figure 4

Calculated heat flux for mold cooling zone, where the mold water flowrate is 530 gpm (0.034 m^3/second) provided by the factory (a); and spray cooling zone (b). Heat flux in spray cooling zone is determined based on spray water flow. Water flowrate provided by the factory at various steady state casting speeds. Linear correlations are fitted to illustrate the relationship between casting speed and spray flux for each spray cooling cage.

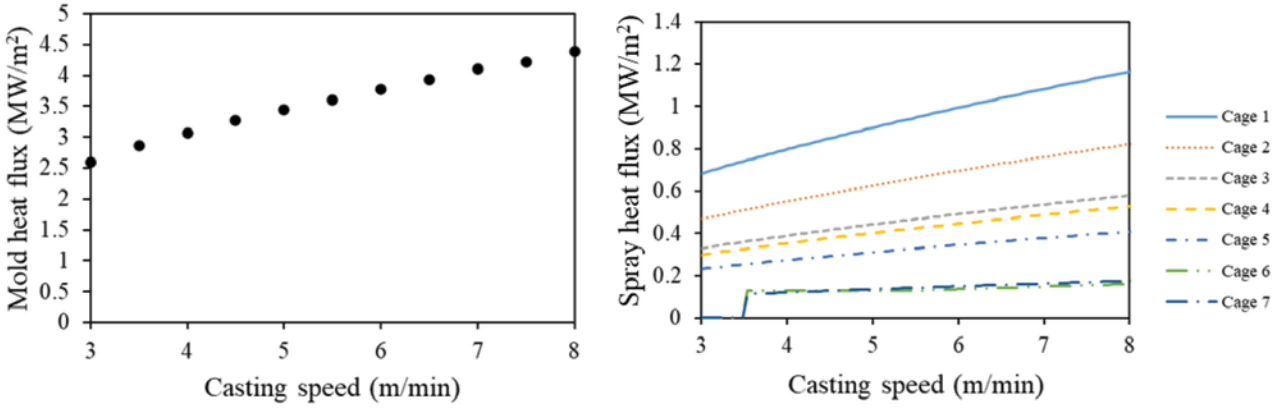

(a) (b)

Table 2

Boundary Conditions for Different Cooling Zones

Cooling zone	Expressions for surface heat flux (W/m^2)	Source	Typical value (MW/m^2)
Mold cooling zone	$\frac{v_w^{Mold}\rho_w C_w \Delta T_w}{L_m W \pi}$	Schwerdtfeger[12]	2
Spray cooling zone	$102,300 * \left(\frac{v_w^{Spray}}{A}\right)^{0.599}$	Fitted from factory data	1
Radiative cooling zone	$Q_{convection} + Q_{radiation}$	Brimacombe[8]	0.5

In Table 2, v_w^{Mold} represents mold water flowrate (m^3/second), ρ_w represents water density (kg/m^3), C_w represents water heat capacity (in J/kg·K), ΔT_w represents mold water temperature change after cooling (K), L_m represents the mold working length (m), W represents the billet diameter (m), v_w^{Spray} represents spray water flowrate, and A represents the billet surface area (m^2).

Steady-State Metallurgical Length Calculations

The first component of the digital twin is a finite difference method (FDM)-based steady-state solidification model. The billet was simulated with a circular cross-section, 73 mm radius based on data provided by an industrial partner. The heat transfer in the billet is described using a numerical solution of Fourier's law (Eq. 1).[8]

$$\rho_s C V \frac{\partial T}{\partial t} = \frac{1}{r}\frac{\partial}{\partial r}\left(kr\frac{\partial T}{\partial r}\right)$$

(Eq. 1)

where

ρ_s (kg/m^3) is the steel density,

C (J/kg·K) is the specific heat,

k (W/m·K) is the thermal conductivity,

r (m) is the radial position in the billet,

T (K) is the temperature and

t (seconds) is the time.

For FDM calculations, the billet is divided into a finite number of nodes, N, where each node point represents the average temperature of a small volume. Uniform temperature was assumed within each node. At each step, the enthalpy for each node was calculated. Other than the center and surface nodes, Eq. 2 is used to calculate volumetric enthalpy for interior nodes.

$$H^{t+1}(i) = H^t(i) + \frac{1}{V_i}\left(S_i\bar{k}_{i,i+1}\Delta t\left(T_{i+1}^t - T_i^t\right) + S_{i-1}\bar{k}_{i,i-1}\Delta t\left(T_{i-1}^t - T_i^t\right)\right), \quad (N > i > 1)$$

(Eq. 2)

where

H^{ti} represents the volumetric enthalpy (J/m^3) at timestep t for node number i,

$\bar{k}_{i,i+1}$ represents the average thermal conductivity between node i and node i+1,

Δt is the timesteps (seconds) that is small enough to satisfied Niyama criterion,

N is the number of nodes and

S_i represents the shape factor (m) for interior nodes which can be calculated through Eq. 3.

$$S_i = \frac{2\pi\Delta r}{\ln\frac{i}{i-1}}, \quad (N > i > 1)$$

(Eq. 3)

In Eq. 3, Δr (m) is the distance between nodes. The enthalpy for the center node is given by Eq. 4.

$$H^{t+1}(1) = H^t(1) + \frac{\Delta t\left(T_2^t - T_1^t\right)}{\frac{\Delta r^2}{4\bar{k}_{1,2}}}$$

(Eq. 4)

Eq. 5 represents the heat extracted from the surface node.

$$H^{t+1}(1) = H^t(1) + \frac{S_{i-1}\bar{k}_{i,i-1}\Delta t\left(T_{i-1}^t - T_i^t\right)}{V_i} + \frac{AW\Delta t}{V_i}$$

(Eq. 5)

where

Q (W/m^2) represents the heat flux to the surroundings and

A is the surface area (m^2).

For steady-state casting boundary conditions, Eq. 6 was used to model convection heat transfer.

$$Q_{convection} = h\left(T_s - T_a\right)$$

(Eq. 6)

where

h is the heat transfer coefficient for convection (W/m^2·K),

T_s (K) is the temperature of the surface node and

T_a (K) is the ambient temperature.

For the convective heat transfer coefficient, a horizontal cylinder model in the air was used where h = 10 W/m^2·K.[9] The radiation heat transfer can be described by the Stefan–Boltzmann law shown in Eq. 7.

$$Q_{radiation} = \epsilon\sigma\left(T_s^4 - T_a^4\right)$$

(Eq. 7)

where

ϵ (0.755) is the emissivity for steel and σ is the Stefan-Boltzmann constant (5.6703 x 10^{-8} W/ m^2·K4).[8]

For a system undergoing a phase change, one approach to determining thermal conductivity and system enthalpy is to couple the system's thermal properties with temperature by computational thermodynamic methods.[8] Thermal conductivity and volumetric enthalpy are determined using CALPHAD software. These properties are then represented as a combination of multiple linear segments based on temperature variations. The CALPHAD calculations are performed using the Thermo-Calc version 2023a with TCFE 13 database.[10] The calculated thermal conductivity and enthalpy at different temperatures are shown in Fig. 5 and Fig. 6.

Surrogate Model for Metallurgical Length Calculations

After constructing the FDM model, the aim is to provide a real-time prediction of metallurgical length at different mold water ΔT (ΔT_w in Table 2) and superheat levels for digital twin usage. To achieve this, it is necessary to develop a surrogate model for faster predictions. For surrogate model construction, first the superheat and mold water ΔT range are obtained from plant operation data. Then, 100 combinations of superheat and mold water ΔT are generated as inputs to simulate 3,700 metallurgical lengths at different casting speeds, along with their corresponding solidification times, to form the training set. Next, this training set is used to feed a multiple linear regression model, generating a surrogate model for metallurgical length and solidification time prediction. The multiple linear regression is carried out by Python with the scikit-learn package.[13]

Results

FDM Model for Steady-State Casting

For validation, the authors compared the simulated surface temperature with plant measurements at two locations: the exit of the water spray zone and just before the induction reheating furnace. The simulation used an industry-provided reference superheat (23 K). At a casting speed of 6.2 m/minute, the simulated surface temperature was 1,379 K, which falls in the pyrometer-measured range of 1,366–1,435 K. Before the induction furnace (51.7 m from the meniscus), the simulated billet surface temperature was 1,258 K, closely matching the observed pyrometer-measured range of 1,227–1,258 K. The surface temperature calculation result is shown in Fig. 7.

To examine surface temperature changes at different casting speeds, the same reference superheat (23 K) was used to simulate the surface temperature at the exit of the spray cooling zone for casting speeds from 3 m/minute to 8 m/minute. The resulting surface temperature at this location is shown in Fig. 8.

In Fig. 8, the water flow in the spray cooling zone varies with changes in casting speed. When the casting speed falls below 4 m/minute, the water flow at the end of the spray cooling zone drops to zero, leading to less surface cooling.

The calculated shell growth at different casting speeds is shown in Fig. 9.

Figure 5

Calculated thermal conductivity of Grade 60 steel (from Thermo-Calc), compared with literature values for AISI-SAE 1025, AISI-SAE 1042, and AISI-SAE 5132 steel.[11]

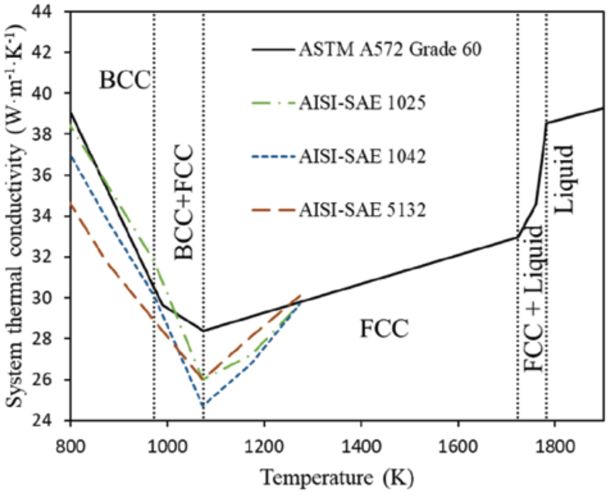

Figure 6

Volumetric enthalpy of Grade 60 steel, calculated with Thermo-Calc.

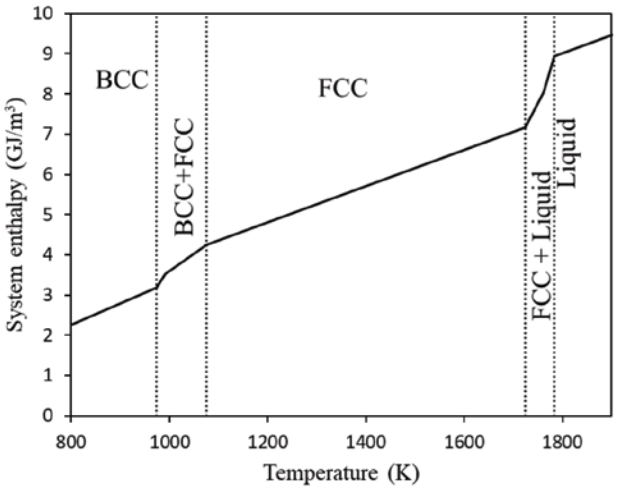

Figure 7

Calculated surface temperatures at casting speeds of 4, 6.2 and 8 m/minute; the boxes marked with dash lines represent the plant pyrometer reading ranges at 6.2 m/minute.

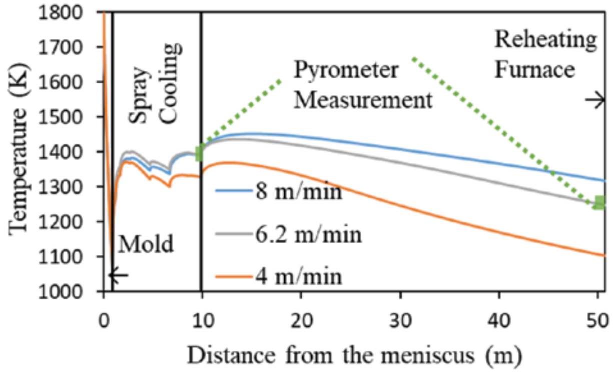

Figure 8

Calculated surface temperature at the exit of the secondary spray zone. Crosses represent the plant pyrometer measurements.

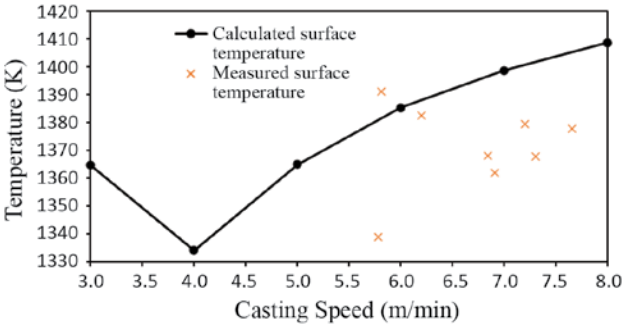

Figure 9

Shell thickness growth for different casting speeds at different positions (a) and different times (b). The cross represents the shell measured from a breakout sample at a casting speed of 5.81 m/minute.

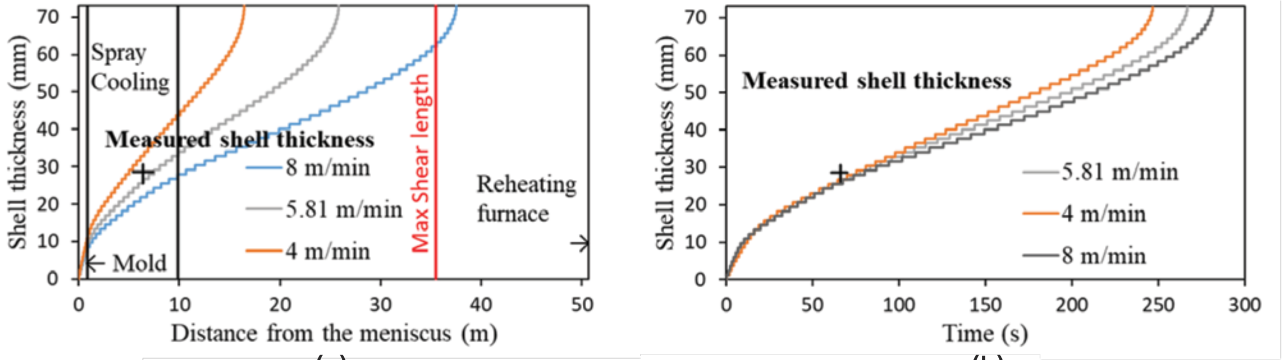

(a)

(b)

The steady-state metallurgical lengths for different casting speeds calculated with the reference superheat (23 K) are shown in Fig. 10.

The calculated metallurgical length was fitted with a polynomial shown in Eq. 8, with v in m/minute and the metallurgical length in m.

$$\mathit{Metallurgical\ Length} = 0.102v^2 + 4v - 0.456 \tag{Eq. 8}$$

The total heat flow across the boundary for steel casting at different casting speeds is shown in Fig. 11.

Figure 10

Calculated metallurgical length at different casting speeds. The plant reference metallurgical length is determined using the supplier-provided casting speed–metallurgical length relationship.

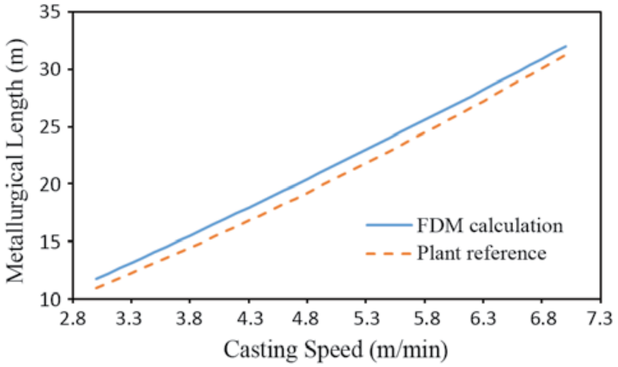

Figure 11

Accumulated heat flows across the billet surface as a function of distance from the meniscus for different casting speeds.

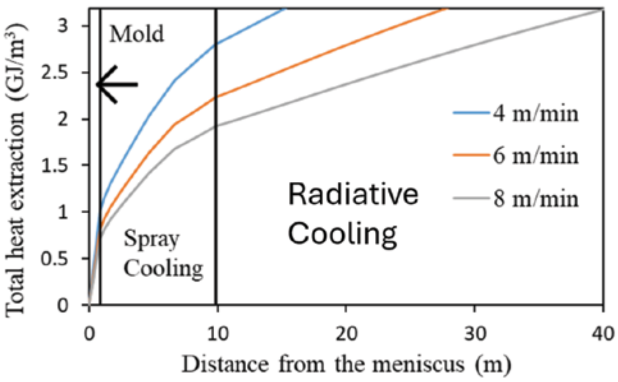

Table 3

Multiple Linear Regression Fitting Result

Dependent variables	Metallurgical length (m)	Solidification time (sec.)
R2	1	0.97
Root mean square error	0.3 m	3.1 sec.
Mean absolute error	0.2 m	2.8 sec.
Casting speed coefficient	5.7 min.	16.9 sec./(m/min.)
Super heat coefficient	0.04 m/K	0.5 sec./K
Mold water ΔT coefficient	–0.8 m/K	–9.5 sec./K
Intercept	5.7 m	236.8 sec.

Surrogate Model for Steady-State Casting

For surrogate model construction, multiple linear regression are used to create two models, both using superheat, mold water ΔT, and casting speed as inputs. One model predicts the metallurgical length, while the other predicts solidification time. The fitting results for both models are shown in Table 3.

Fig. 12 shows the metallurgical length prediction results and the corresponding residuals from the surrogate model.

Fig. 13 shows the solidification time prediction results and the corresponding residuals from the surrogate model.

The calculation time for a single solidification simulation is 7 seconds for the FDM model and 1.5 milliseconds for the surrogate model. For metallurgical length calculation, the FDM model also takes 7 seconds, while the surrogate model requires 5 milliseconds.

Discussion

Fig. 5 shows that the thermal conductivity of CALPHAD-calculated Grade 60 steel is similar to the values reported in the literature for low- to medium-carbon steels at low temperatures. This indicates that the CALPHAD calculation is a reliable method for determining thermal conductivity and enthalpy.

As shown in Fig. 7, at high casting speeds, the surface temperature at the exit of the secondary spray zone is less affected by casting speed. Specifically, at 6.2 m/minute and 8 m/minute, the surface temperatures in the last spray cage are almost identical, suggesting that at high casting speeds, the water spray setting balanced the effect of shell thickness. At 4 m/minute, the surface temperature differs significantly from the two higher-speed cases due to longer solidification time. When the casting speed

Figure 12

Multiple linear fitting of metallurgical length: Actual vs. predicted values (a) and prediction residuals (b).

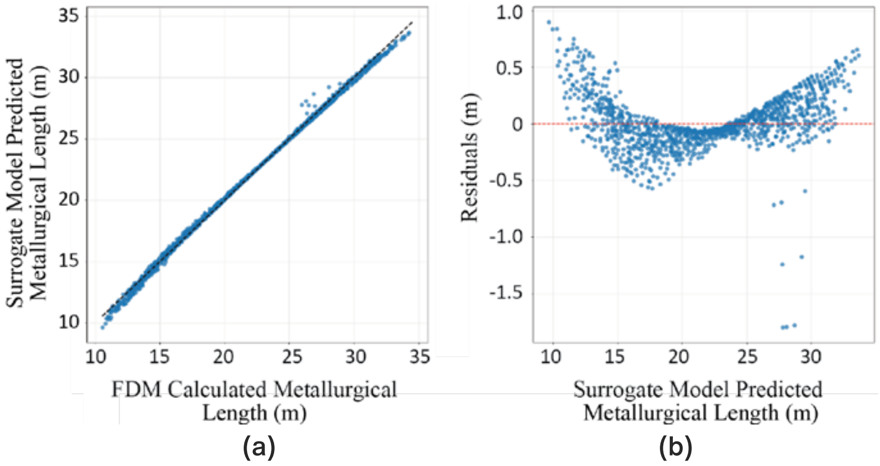

Figure 13

Multiple linear fitting of solidification time: Actual vs. predicted values (a) and prediction residuals (b).

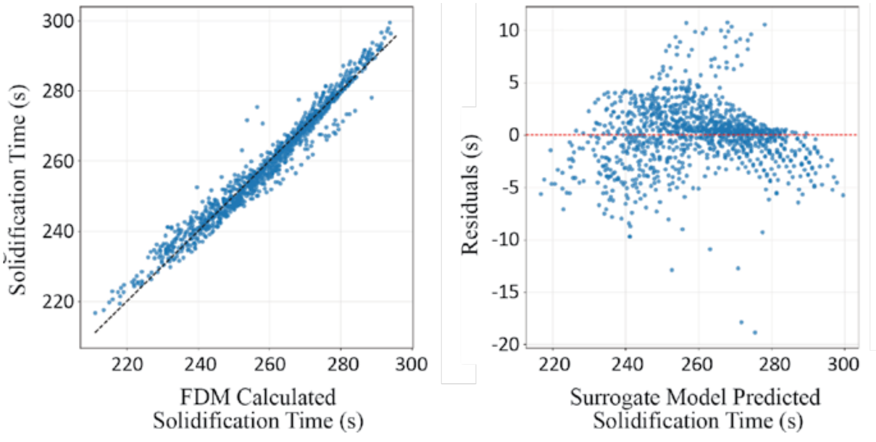

(a) (b)

is below 3.5 m/minute, the plant stops spraying in the last two cages, leading to a significantly higher surface temperature.

The calculated surface temperatures generally fall in the range of actual pyrometer reading. Differences can rise because pyrometers have a high degree of uncertainty under the difficult measuring conditions at the spray zone exit, and the superheat is not always equal to the reference superheat used in the calculations.

Fig. 9a shows the shell thickness growth as the billet travels along the caster. At the maximum casting speed of 8 m/minute, the metallurgical length exceeds the maximum shear length, meaning that shearing the billet at 8 m/minute would result in a breakout at the shearing position. From Fig. 9b, it is observed that although the three casting speeds have different heat extraction rates in mold and spray cooling zones, their solidification times are not significantly different. Specifically, at 4 m/minute, the solidification time is only 50 seconds shorter than that at 8 m/minute. In contrast, shell thickness growth along the travel distance varies more significantly between different casting speeds. This suggests that the primary factor influencing metallurgical length variation is differences in travel distance rather than solidification time, which remains relatively similar across speeds. While water spray does impact solidification time, it is not the dominant factor in metallurgical length changes. To further support this understanding, the cumulative heat extraction from the billet was plotted in Fig. 11. The results show that at low casting speeds, most of the heat is removed before the billet exits the secondary cooling zone, indicating that water spray plays a greater role in shell formation. However, at high casting speeds, up to 45% of the heat is extracted in the radiation cooling zone before solidification is completed. This suggests that at higher speeds, water spray contributes more to maintaining a uniform surface temperature rather than enhancing heat extraction.

Table 3 shows that both the metallurgical length prediction surrogate model and the solidification time prediction model provide a good fit.

Conclusion

In summary, this study presents a draft framework for a digital twin partially designed for a micro-mill caster, along with implementation methods for each component.

This investigation into casting speed effects shows that at high speeds, the surface temperature near the spray cooling zone exit is primarily influenced by water spray, whereas at low casting speeds, billet travel time plays a more significant role. The validated shell thickness predictions reinforce the accuracy of the model, particularly in identifying the risk of billet breakout at the shearing position at high casting speeds. Furthermore, this study demonstrates that while water spray affects solidification time, it is not the dominant factor in metallurgical length variation for high-speed casters. Instead, differences in travel time at varying casting speeds are the primary contributors. The heat flow analysis confirms that at low casting speeds, most cooling occurs within the spray cooling zone, whereas at higher speeds, a significant portion of heat extraction shifts to the radiation-cooling zone.

The integration of machine learning for metallurgical length prediction significantly improves prediction speed. With a calculation time of less than 5 milliseconds, real-time steady-state metallurgical length prediction is feasible while the caster is running. The results indicate that both the solidification time prediction surrogate model and the metallurgical length surrogate model provide accurate predictions.

For future research, the authors plan to integrate the surrogate model into transient speed cases. As casting speed changes, the authors' surrogate model could predict real-time steady-state solidification time, which would then serve as a boundary condition to calculate metallurgical length variations during transient states.

References

1. R.I.L. Guthrie and M.M. Isac, “Continuous Casting Practices for Steel: Past, Present and Future,” *Metals,* Vol. 12, No. 5, May 2022, doi: 10.3390/met12050862.
2. “Comparison of Continuous Strip Casting With Conventional Technology,” accessed 6 February 2025, https://www.jstage.jst.go.jp/article/isijinternational1989/43/8/43_8_1115/_article.
3. T. Watanabe, “Overview of Near-Net-Shape Continuous Casting for Steel Sheet,” *Tetsu-to-Hagané,* Vol. 88, No. 3, pp. 107–116, 2002, doi: 10.2355/tetsutohagane1955.88.3_107.
4. A.N. Smirnov and S.V. Kuberskii, “Continuous Casting of Steel at Micro Mills,” *Steel Transl.,* Vol. 46, No. 2, 2016, pp. 132–137, doi: 10.3103/S0967091216020145.
5. A. Thelen et al., “A Comprehensive Review of Digital Twin — Part 1: Modeling and Twinning Enabling Technologies,” 2022, arXiv: arXiv:2208.14197. doi: 10.48550/arXiv.2208.14197.
6. A.L. Hananto et al., “Digital Twin and 3D Digital Twin: Concepts, Applications, and Challenges in Industry 4.0 for Digital Twin,” *Computers,* Vol. 13, No. 4, Art. No. 4, 2024, doi: 10.3390/computers13040100.
7. S.M. Bazaz, M. Lohtander and J. Varis, “5-Dimensional Definition for a Manufacturing Digital Twin,” *Procedia Manuf.,* Vol. 38, 2019, pp. 1705–1712, doi: 10.1016/j.promfg.2020.01.107.
8. J.K. Brimacombe, “Design of Continuous Casting Machines Based on a Heat-Flow Analysis: State-of-the-Art Review,” *Can. Metall. Q.,* Vol. 15, No. 2, 1976, pp. 163–175, doi: 10.1179/000844376795050796.
9. T. Yener, Ş.Ç. Yener and R. Mutlu, “Convection Coefficient Estimation of Still Air Using an Infrared Thermometer and Curve-Fitting,” *J. Eng. Technol. Appl. Sci.,* Vol. 4, No. 2, Art. No. 2, 2019, doi: 10.30931/jetas.598862.
10. “Steel and Fe-Alloys – TCFE,” Thermo-Calc Software, accessed 9 February 2025, https://thermocalc.com/products/databases/steel-and-fe-alloys.
11. *Properties and Selection: Irons, Steels, and High-Performance Alloys,* ASM International, 1990, doi: 10.31399/asm.hb.v01.9781627081610.
12. K. Schwerdtfeger, “Heat Withdrawal in the Mold in Continuous Casting of Steel: Review and Analysis,” *Steel Res. Int.,* Vol. 77, No. 12, 2006, pp. 911–920, doi: 10.1002/srin.200606481.
13. F. Pedregosa et al., “Scikit-learn: Machine Learning in Python,” *J. Mach. Learn. Res.,* Vol. 12, No. 85, 2011, pp. 2825–2830.

✦

AISTech The original version of this paper was presented at AISTech 2025 — The Iron & Steel Technology Conference and Exposition, Nashville, Tenn., USA, and published in the AISTech 2025 Conference Proceedings.